Effect of thermo-mechanical treatments on corrosion behavior of Cu-15Ni-8Sn Alloy in 3.5 wt% NaCl solution

Yang Zhang [a], Zhu Xiao [a,b,*], Yuyuan Zhao [c], Zhou Li [a,d,*], Yan Xing [a], Kechao Zhou [b]

[a] School of Materials Science and Engineering, Central South University, Changsha, 410083, China

[b] State Key Laboratory of Powder Metallurgy, Changsha, 410083, China

[c] School of Engineering, University of Liverpool, Liverpool, L69 3BH, UK

[d] Key Laboratory of Nonferrous Metal Materials Science and Engineering, Ministry of Education, Changsha, 410083, China

Abstract: The microstructure and corrosion behavior of the Cu-15Ni-8Sn-1.0Zn-0.8Al-02Si alloy treated with different thermo-mechanical processes in 3.5 wt% NaCl solution was investigated by electrochemical test, electron microscopy and XPS analysis. Compared with single-stage thermo-mechanical treatment (cold rolling by 60% reduction and then aging at 450℃ for 0.5h), the alloy with two-stage treatment (pre-aging at 400℃ for 0.5h, cold rolling by 60% reduction and then aging at 450℃ for 0.5h) had finer ordered precipitates and less coarse, discontinuous precipitates, resulting in better corrosion resistance performance. The corrosion product layer was mainly a mixture of Cu_2O, CuO, NiO, $Ni(OH)_2$, SnO, SnO_2, ZnO and Al_2O_3, with a transition from Cu_2O to CuO and $Cu(OH)_2$ occurring during the corrosion process.

Keywords: Alloy; Polarization; XPS; Thermo-mechanical treatments;

*Corresponding authors: Tel(Fax): +86 731 88830236, E-mail address: xiaozhumse@163.com (Z. Xiao);
Tel: +86 731 88830264, Fax: +86 731 88876692, E-mail address: lizhou6931@163.com (Z. Li).

1.Introduction

Cu-Ni-Sn alloys have been widely used in deep sea pipelines, bearings and electronics in marine engineering, due to their high strength, excellent corrosion resistance and good resistance to stress relaxation at high temperature [1-3]. Many studies have been conducted on the structure, phase transformation and mechanical properties of the Cu-Ni-Sn alloys. It was revealed that the segregation of Sn and some brittle Sn-rich phases in the alloy has a detrimental effect on the properties of the alloy [4]. Changing alloy composition and/or applying appropriate heat treatments on the alloy can be effective in hindering the Sn segregation and the precipitation of some Sn-rich phases, and therefore lead to more homogeneous structure and improved mechanical properties and corrosion resistance [4-6]. Deyong *et al* [7] investigated the electrochemical behavior of rapidly solidified Cu-Ni-Sn alloys with different contents of nickel and tin. They found that the corrosion resistance decreased when the Ni content was decreased from 15 to 10% and when the Sn content was increased, and the precipitation of nickel and tin rendered the matrix less noble with respect to any γ phase present, making the matrix more vulnerable for corrosion [7]. Heat treatment was also found to affect the corrosion behavior of the alloy due to precipitation of secondary phases, as different precipitation configuration changed the chemical homogeneity of the matrix [8-10].

Cu-15Ni-8Sn, a typical spinodal-decomposition-strengthened alloy, has gathered a considerable amount of interest as it possesses good combination of strength, elastic modulus and electrical conductivity, making it a good candidate as a spring and anti-wear material [11-13]. Recently, researches about the Cu-Ni-Sn alloy mainly focused on its phase transformation, improvement of strength properties and wear resistance

[14-17]. However, there is very little work reported in the literature on its' corrosion behavior. In the present work, a new Cu-15Ni-8Sn-based alloy was prepared with additions of Zn, Si and Al. Zn was added to improve the quality of the ingot by reducing casting pinholes and cracks. Si and Al were added in order to impede the cellular precipitation of γ' phase at grain boundaries and to improve the strength and corrosion resistance of the alloy. Single- and two-stage thermo-mechanical treatments were applied in the aging process. The microstructure and corrosion behavior of the alloy with these two thermo-mechanical treatments were investigated.

2.Experimental Procedures

2.1 Sample Preparation

The main alloying elements of the Cu-15Ni-8Sn-based alloy are listed in Table 1. The alloy was prepared by induction melting and mold casting. After the removal of surface defects, the ingot was homogenized at 830℃ for 4h, and then hot rolled with a reduction of 70%. The hot rolled alloy was solution-treated at 850℃ for 1h, followed by water quenching. Two different thermo-mechanical treatments were applied to the solution-treated samples: 1) two-stage thermo-mechanical treatment (TTMT) - pre-aging at 400℃ for 0.5h, cold rolling by 60% reduction, and then aging at 450℃ for 0.5h; 2) single-stage thermo-mechanical treatment (STMT) - cold rolling by 60% reduction and then aging at 450℃ for 0.5h. Specimens with the dimensions of 50mm×25mm×1.2mm were cut from the TTMT and STMT samples by wire-electrode cutting. All cut specimens were mechanically ground, polished, ultrasonically cleaned in alcohol, degreased in acetone and rinsed with deionized water before immersion test.

Element	Cu	Ni	Sn	Al	Si	Zn
Concentration	Balance	15	8	0.8	0.2	1.0

Table1 Chemical composition of the designed alloy (wt%)

2.2 Electrochemical Test

The specimens used for electrochemical test were exposed in 3.5wt% NaCl solution at 30℃ for 1, 3, 7, 15 and 30 days. Dental base acrylic resin powder and liquid were used to seal the surface of each specimen, leaving an uncovered area of 1×1 cm^2 for test. The direct current (DC) electrochemical test was conducted on an IM6ex electrochemical workstation (Zahner Co., Germany) at room temperature, using Pt as the auxiliary electrode and saturated calomel electrode (SCE) as the reference electrode. The variations of the open-circuit potential (OCP) with time for STMT and TTMT samples are shown in Fig.1. The open-circuit potential of both samples reached the steady state at about 2600 s, with the open-circuit potential of 24.5±0.8 mV_{SCE} for the STMT sample and 21.1±1.5 mV_{SCE} for the TTMT sample. The potential-dynamic polarization measurements were conducted by scanning from -0.2 V to 0.8 V with a speed of 1mV/s and the data were analyzed by the CHI660C software. Because DC electrochemical tests and polarization curves can only provide information on the overall corrosion of the alloy, electrochemical impedance spectroscopy (EIS) analysis was used to investigate the structure of the corrosion layer in the TTMT samples. For EIS measurements, the signal amplitude of the AC voltage was 20 mV (peak to zero) and the frequency was between 100 kHz and 10 MHz. The experimental data was analyzed by the Z-view software. All the electrochemical tests were carried out in the same corrosion medium after the open circuit potential (OCP) was stabilized.

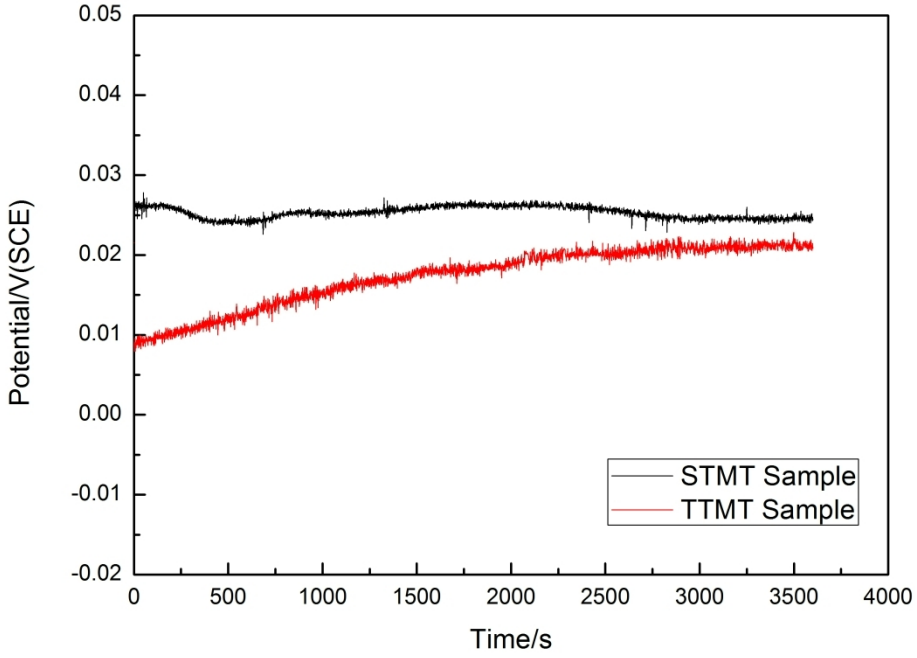

Figure 1 Open circuit potential curves of (a) TTMT and (b) STMT specimens exposed in 3.5wt% NaCl solution.

2.3 Microstructure Observation and Analysis

The microstructures of the TTMT and STMT samples without corrosion were observed on a Tecnai G2 F20 transmission electron microscope (TEM) (FEI Co., Holland). The TEM specimens, 3mm in diameter, were prepared by twin-jet electro-polishing in a 30vol% nitric acid and 70vol% methanol solution at -30℃. The morphology and thickness of the corrosion layers of the TTMT and STMT specimens, after exposed in 3.5wt% NaCl solution for 30 days, were observed and the energy dispersive X-ray (EDX) analysis was carried out on a Siron 200 scanning electron microscope (SEM) equipped with EDAX GENESIS 60 (FEI Co., Holland). The SEM specimens were rinsed with deionized water and air dried before observation.

2.4 X-ray Photoelectron Spectroscopy Analysis

The X-ray Photoelectron Spectroscopy (XPS) of TTMT specimens exposed in the 3.5wt% NaCl solution at 30℃ for 1 day and 30 days was carried out on a K-Alpha 1063 X-ray photoelectron spectroscope (Thermo-Fisher Scientific Co., USA), with a monochromotized Al-K_α X-ray source in vacuum of 10^{-9} mBar. The outputs were recorded as bonding energy vs. intensity count plots. The experimental data of the XPS were analyzed by the XPS PEAK software and the best fit was obtained by a non-linear least square regression method.

3.Results and Discussion

3.1 Polarization Curves

Figure 2 shows the polarization curves of the TTMT and STMT specimens exposed in 3.5wt% NaCl solution for different times. The corrosion current densities increased with increasing potential in the anodic curves. A passive region was observed in all specimens, suggesting the formation of a protective oxide film on the surface of the specimens [18-21].

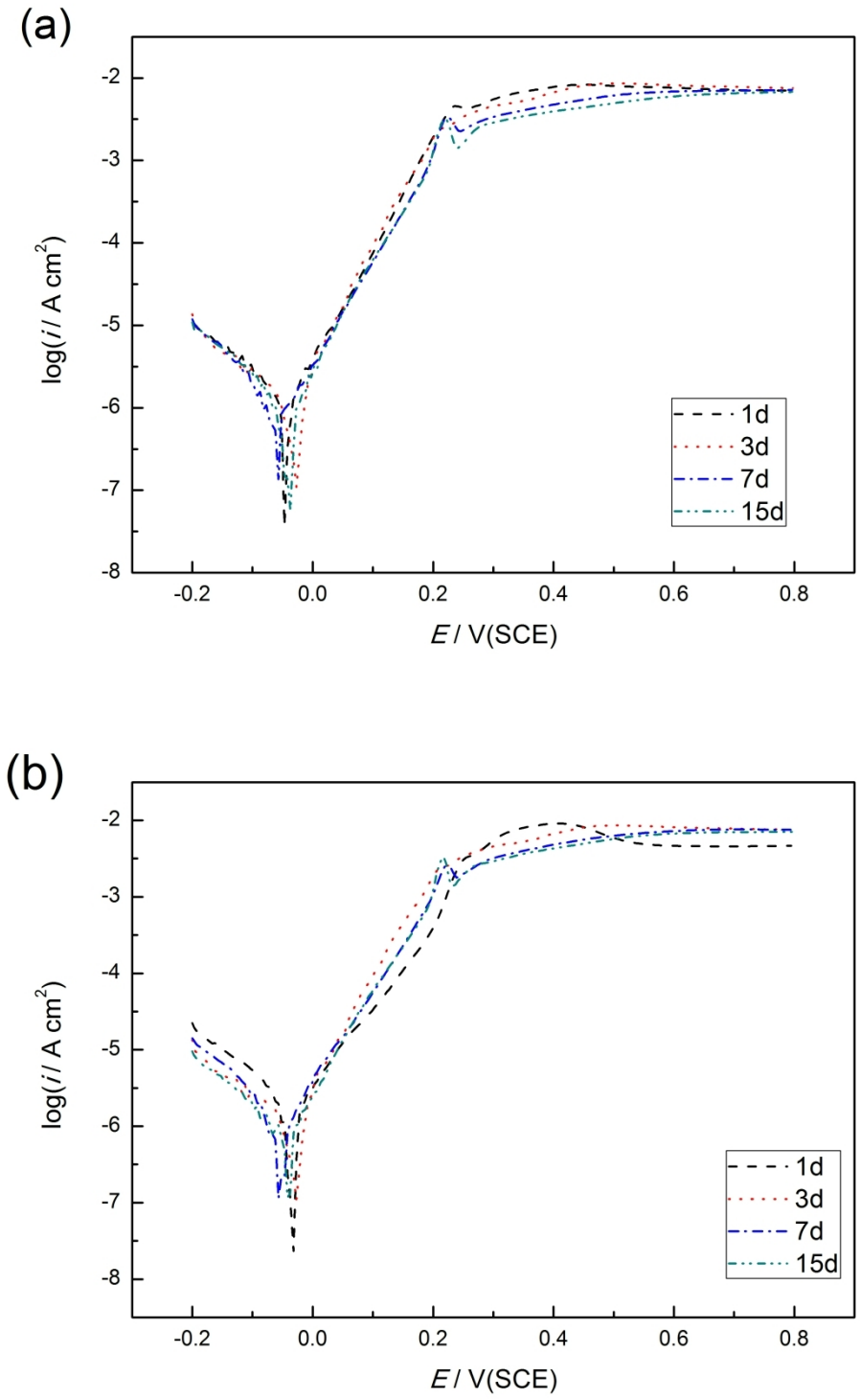

Figure 2 Polarization curves of (a) TTMT and (b) STMT specimens after exposed in 3.5wt% NaCl solution for different times.

The electrochemical parameters obtained from the polarization curves are shown in Table 2. The polarization resistance, R_p, was calculated by the Stern-Geary equation:

$$\beta_p = \frac{\beta_a \times |\beta_c|}{2.303(\beta_a + |\beta_c|) \times i_{corr}}$$

where β_a and β_c are the anode and cathode Tafel slopes, respectively, E_{corr} is the corrosion potential and i_{corr} is the corrosion current density.

Sample	Exposure time (days)	β_a (mV/Dec^{-1})	β_b (mV/Dec^{-1})	E_{corr} (V)	i_{corr} (μA•cm^{-2})	R_p (KΩ•cm^2)
TTMT	1	73.73	-176.08	-0.032	1.22	18.52
	3	65.68	-183.29	-0.029	1.062	19.80
	7	98.71	-135.09	-0.059	1.088	22.79
	15	69.83	-131.17	-0.039	0.706	28.06
STMT	1	109.90	-191.87	-0.029	2.39	12.71
	3	105.68	-184.84	-0.028	2.22	13.17
	7	97.85	-138.02	-0.055	1.31	19.00
	15	77.93	-171.04	-0.040	0.96	24.20

Table 2 Electrochemical parameters of the polarization curves of the TTMT and STMT specimens after exposed in 3.5wt% NaCl solution for different times.

The corrosion current density of both TTMT and STMT specimens changed with exposure time in a similar pattern. The corrosion current densities decreased with corrosion time, suggesting the formation of a protective oxide film on the surface of the specimens [20,21]. After immersed in 3.5wt% NaCl solution for 15 days, the equivalent resistance, R_p, of the TTMT sample increased from 18.52 to 28.06 kΩ•cm^2,

while that of the STMT sample from 12.71 to 24.20 kΩ•cm^2. The TTMT sample had a smaller corrosion current density and a larger polarization resistance than the STMT sample for all given exposure times, suggesting that the TTMT sample has better corrosion resistance performance.

3.2 Microstructure

3.2.1 SEM observation of corrosion layer

Figure 3 shows the SEM images of the cross sections and surfaces of the TTMT and STMT samples exposed in 3.5wt% NaCl solution for 30 days. After exposure for 30 days, a corrosion film formed on the surface of both samples. The corrosion product layer on the TTMT sample was uniform with a straight interface (Fig. 3a). In contrast, the corrosion product layer on the STMT sample had a variable thickness and an uneven interface with the matrix (Fig. 3c). The film on the surface of TTMT is dense and uniform (Fig. 3b). The film on the surface of STMT, however, is relatively rough (Fig. 3d) and shows some corrosion pits (indicated by red arrow), suggesting additional attack by localised corrosion. Severe localised corrosion is often related to non-uniform microstructure and non-uniform distribution of second phases [5]. These observations suggested that the TTMT treatment produced better microstructure than the STMT treatment and therefore improved the corrosion resistance performance of the alloy.

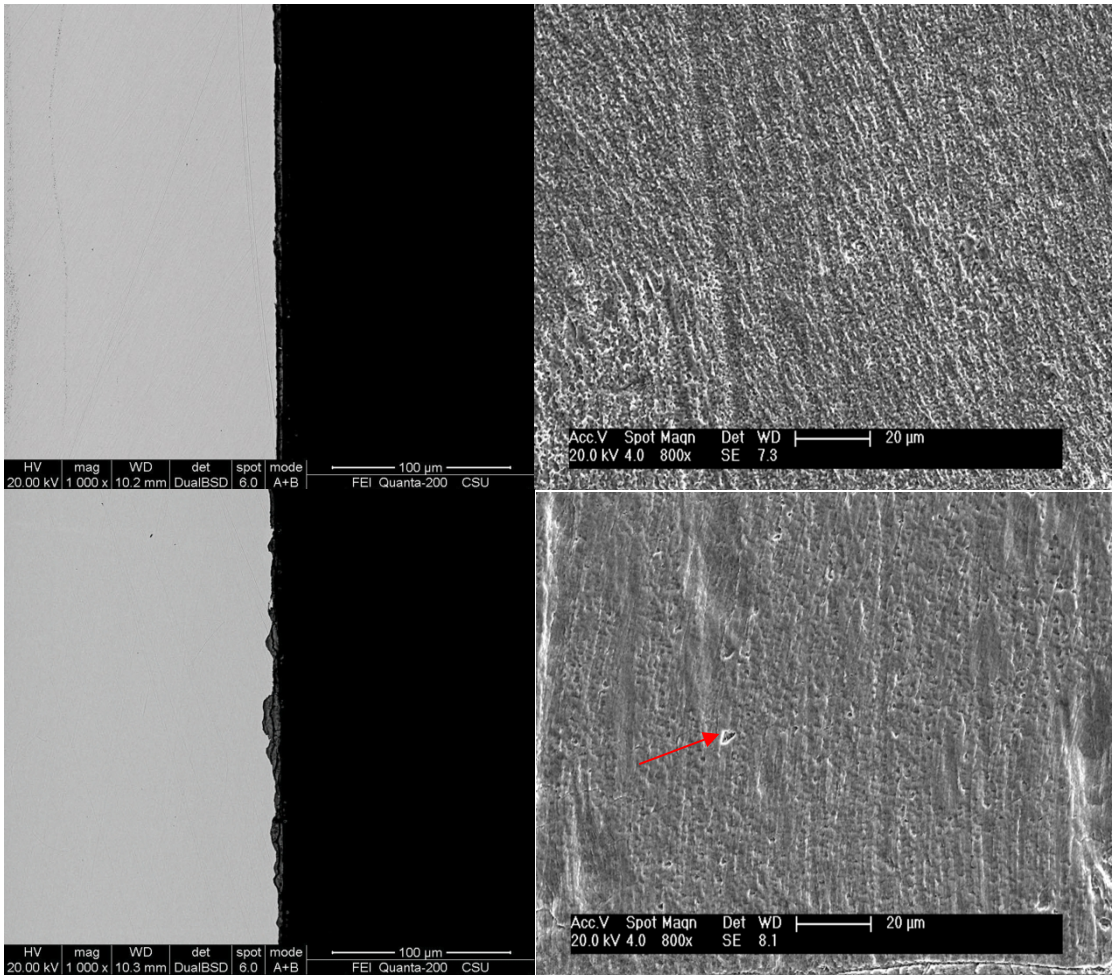

Figure 3 SEM images of samples exposed in 3.5wt% NaCl solution for 30 days: (a) cross section of TTMT; (b) surface of TTMT; (c) cross section of STMT; (d) surface of STMT.

3.2.2 EDX analysis of corrosion layer

Fig. 4 shows the EDX analysis results of the corrosion product layer of the TTMT and STMT samples exposed in 3.5wt% NaCl solution for 30 days. The concentrations of the elements were calculated by taking average values of five EDX analyses of the corrosion film along the interface. The corrosion product layer mainly contained Sn, Ni, Cu, O, Al, Zn and Si. The corrosion product layer was deficient of Cu, while the concentrations of the alloying elements were far higher than those in the matrix. It may be speculated that insoluble oxides of the alloying elements formed by corrosion

remained in the corrosion layer, while much of Cu was transformed to Cu^{2+} and Cu^{+} and was dissolved in the solution. The difference of Cu in TTMT and STMT samples after corrosion were more likely attributed to localized corrosion in the STMT sample. Since the existence of uneven distributed precipitates led higher corrosion speed, the STMT sample had lower concentration of Cu.

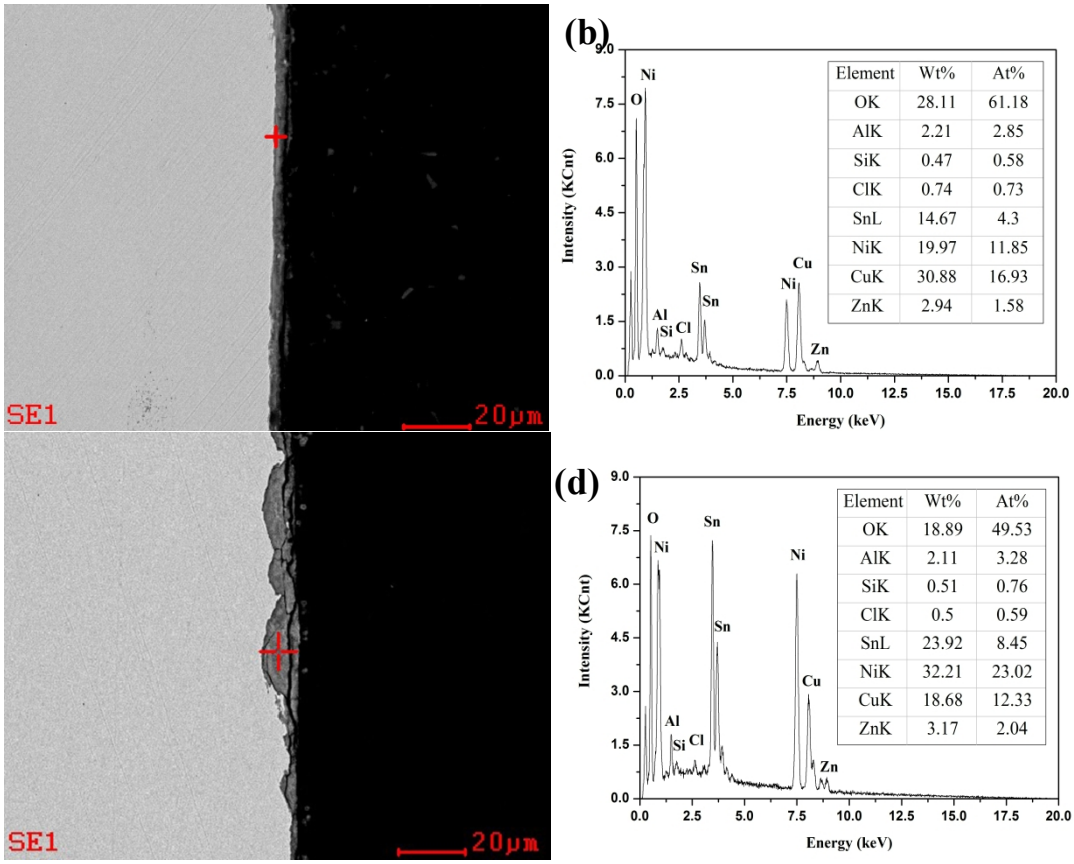

Figure 4 EDX analysis results of the corrosion product layer of samples immersed in 3.5wt% NaCl solution for 30 days: (a) SEM and (b) elemental concentrations for the TTMT sample; (c) SEM and (d) elemental concentrations for the STMT sample.

There were no discernible differences in the concentrations of the alloying elements Al, Si, Zn and Cl between the TTMT and STMT samples. However, the concentrations of elements Ni and Sn in the STMT sample were much higher than those in the TTMT samples, suggesting preferential corrosion of Sn and Ni rich areas

(e.g., γ phase) in the STMT samples [13,22]. The element O was mainly present in insoluble oxides and hydroxides, the main corrosion products on the surface of the alloy. Compared with the STMT sample, the O concentration in the TTMT sample was much higher, indicating much denser oxides and hydroxides.

3.2.3 TEM analysis of aged alloy

Cu-15Ni-xSn (x=3-15wt%) alloys could have at least six types of precipitation reactions, including spinodal decomposition, ordered micro-precipitates DO_{22}/LI_2 $(Cu_xNi_{1-x})_3Sn$, discontinuous cellular γ phase, and continuous precipitation of γ phase and δ phase [11].

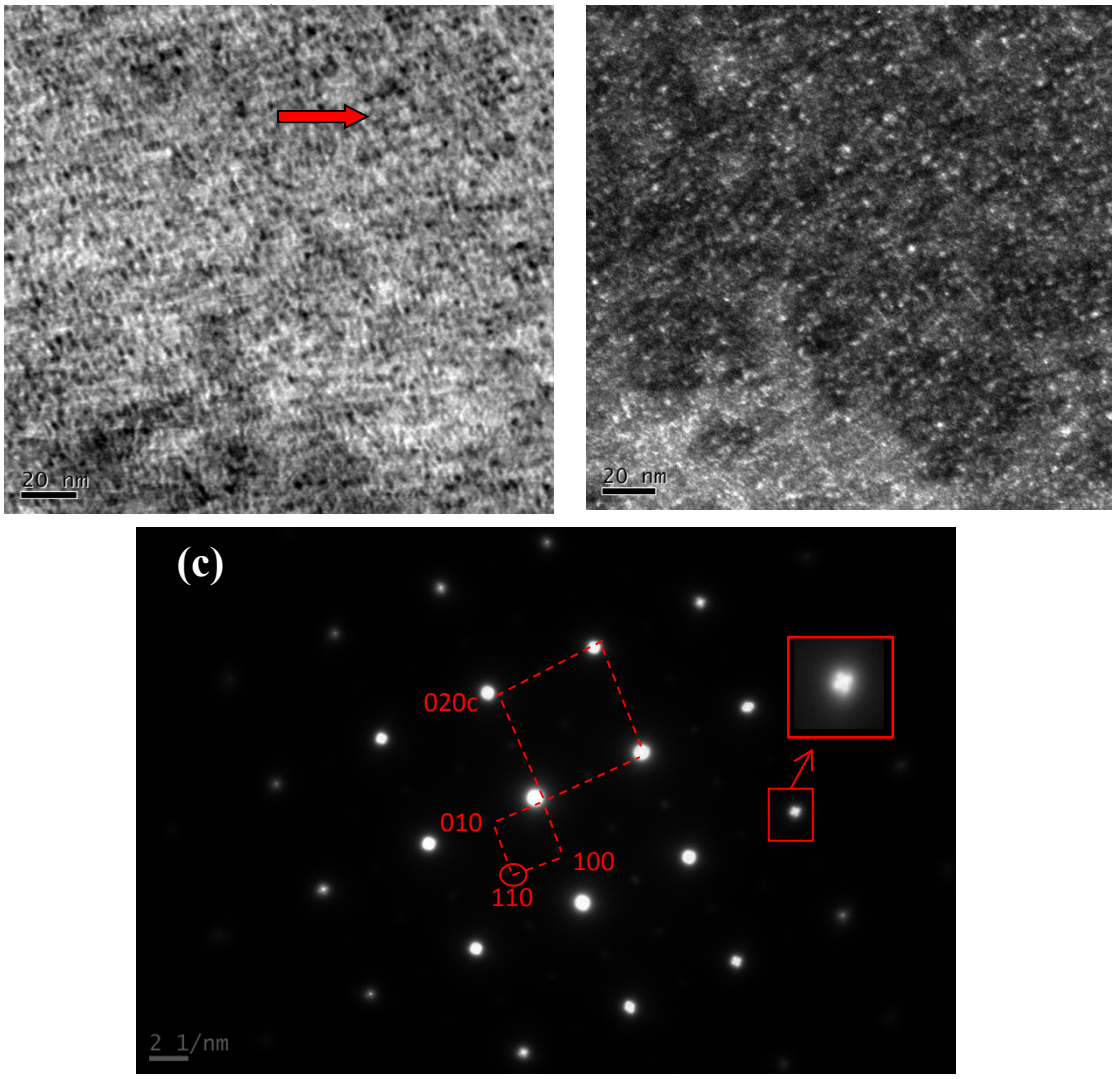

Fig 5 (a) Bright field and (b) Dark field TEM micrographs of the alloy pre-aged at 400℃

Fig. 5 shows the TEM micrographs and the selected area diffraction patterns (SADPs) of the alloy pre-aged at 400℃ for 0.5 h. The bright field image (Fig. 5a) shows a basket structure from spinodal decomposition with nano-scale dark phases (marked with arrow). The dark field image (Fig. 5b) shows the super-lattice reflections with the nano-scale phases (bright) clearly seen. Fig. 5c is the corresponding SADPs of Fig. 5a, with the electron beam parallel to $[100]_{cu}$. The spots of the super-lattice reflections of the matrix were indexed and the satellite diffraction spots around {200} coming from the spinodal decomposition were recorded (marked with arrow). According to the SADPs results (Fig. 5c), the precipitates were ordered-precipitates of $(Cu_xNi_{1-x})_3Sn$.

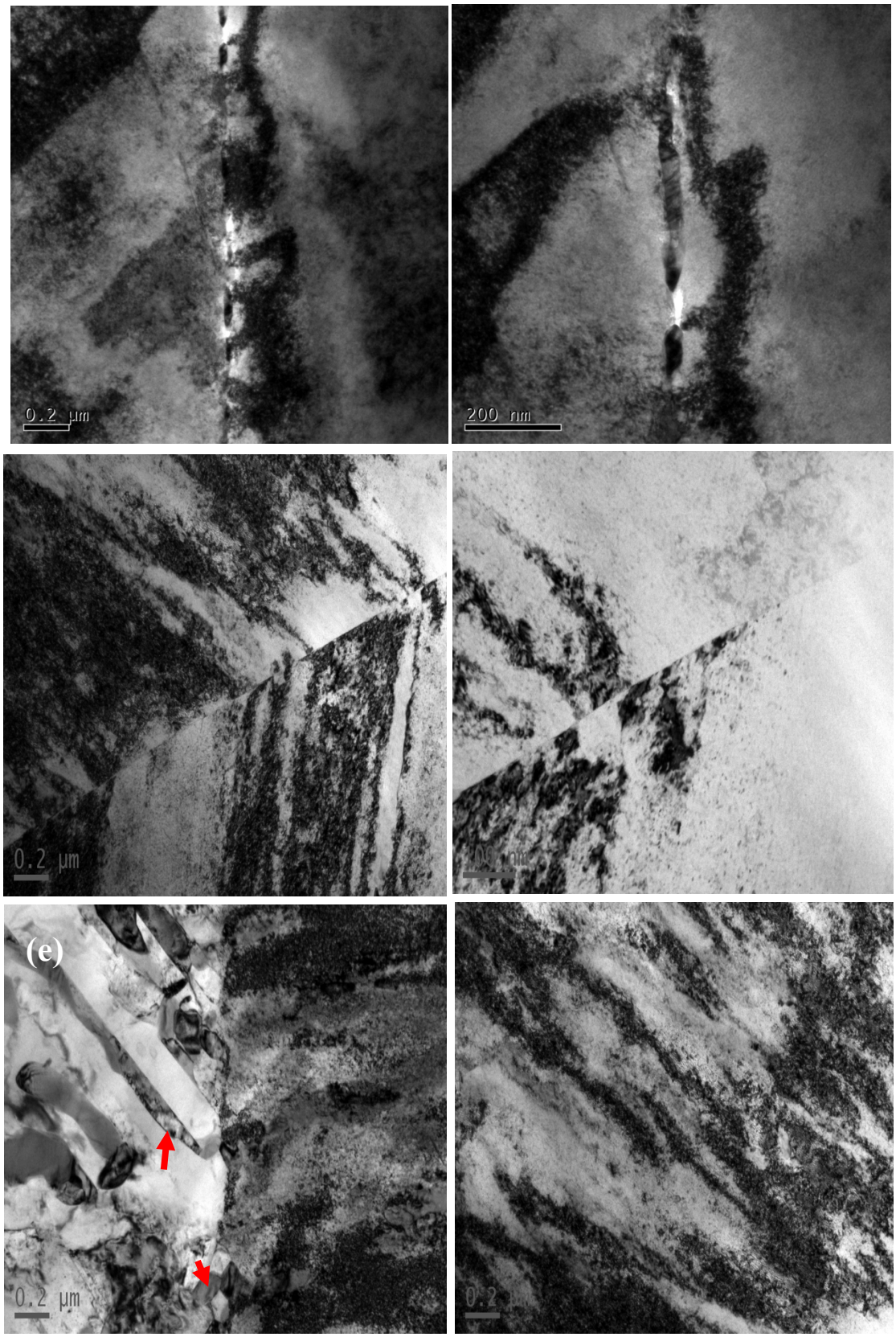

Figure 6 Bright field TEM micrographs of (a, b) STMT sample (cold rolling by 60% reduction and then aging at 450℃ for 0.5h), (c, d) TTMT sample (pre-aging at 400℃

for 0.5h, cold rolling by 60% reduction, and then aging at 450℃ for 0.5h), (e) discontinuous precipitation (cellular) γ phase in STMT sample, and (f) dislocation tangles in TTMT sample

Fig. 6 shows typical TEM images of the grain boundaries of the STMT and TTMT samples. There were coarse discontinuous precipitation phases on the grain boundaries in the STMT sample (Fig. 6a and b), which was in accordance with previous studies [11,23]. Few discontinuous precipitation phases were found in the TTMT sample (Fig. 6c and d). The hinder of the formation of discontinuous precipitation at grain boundaries could be attributed to the decreased solutes in the matrix due to the spinodal decomposition and the formation of ordered micro-precipitates during pre-aging.

The discontinuous precipitation phases were the early stage of discontinuous cellular γ phase rich of Sn [23-24]. When the aging time was increased to 8h (60%+450℃×8h), these discontinuous precipitates developed from the grain boundaries into the matrix (marked with arrow in Fig. 6e). The Sn-rich discontinuous precipitates acted as anode while the Cu matrix acted as cathode, forming galvanic micro-batteries between small anodes and a large cathode. These micro-batteries would accelerate the corrosion process [25,30], making the alloy more susceptible to localised corrosion as observed in the SEM photographs (Fig. 3c).

In the TTMT sample, the ordered nano-scale precipitates formed during pre-aging (marked by arrow in Fig. 5a) interacted with the dislocations during the subsequent cold deformation process, forming dense dislocation tangles (Fig. 6f). These

dislocation tangles provided a large number of nucleation locations during the subsequent aging process, leading to uniform distribution of fine precipitates [13]. These uniformly distributed precipitates in the TTMT sample could make a contribution to a finer uniform distribution of chemical elements which was helpful to form a continuous and homogeneous corrosion layer and thus improved the corrosion resistance of the alloy.

3.3 Sub-Processes of Corrosion and Corrosion Products in TTMT Samples

3.3.1 EIS analysis

Figure 7 shows the electrochemical impedance spectra of the TTMT samples exposed in 3.5 wt% NaCl solution for different times at 30℃. The Nyquist curves in Fig. 7a are nearly linear in the low frequency zone, evidencing a diffusion impedance characteristic (Warburg diffusion impedance). Typical semicircle shapes of Nyquist plots follow and the diameters of the semicircles increase with exposure time, indicating increases in the transfer resistance and the oxide film resistance with exposure time. The total impedance Bode plots (Fig. 7b) show that log|Z| in the low frequency zone increased with exposure time from 1 to 15 days, indicating that the protective corrosion film grew thick. When the exposing time was further prolonged to 30 days, however, there was little change of log|Z| and the capacitive behavior disappeared in the low frequency zone, suggesting that the diffusion process was dominant [18-20]. In the medium frequency zone (log$f$ = 0-4), there is a linear relationship between log|Z| and log$f$, with a gradient of -1, due to the capacitive nature of the electrical double layer (EDL). The high frequency zone (log$f$ = 4-5) shows the typical impedance characteristics of solution resistance. In the Bode phase angle plots (Fig. 7c), the 1-day specimen shows one peak while the 7-, 15- and 30-day specimens

show two peaks, although the peak at the higher frequency is not as prominent as the one at the lower frequency and generally decreases with exposure time. The phase angle peak in the low frequency zone was due to the EDL. The peak in the high frequency zone could be attributed to the formation of a multilayer, non-protective corrosion product film [21].

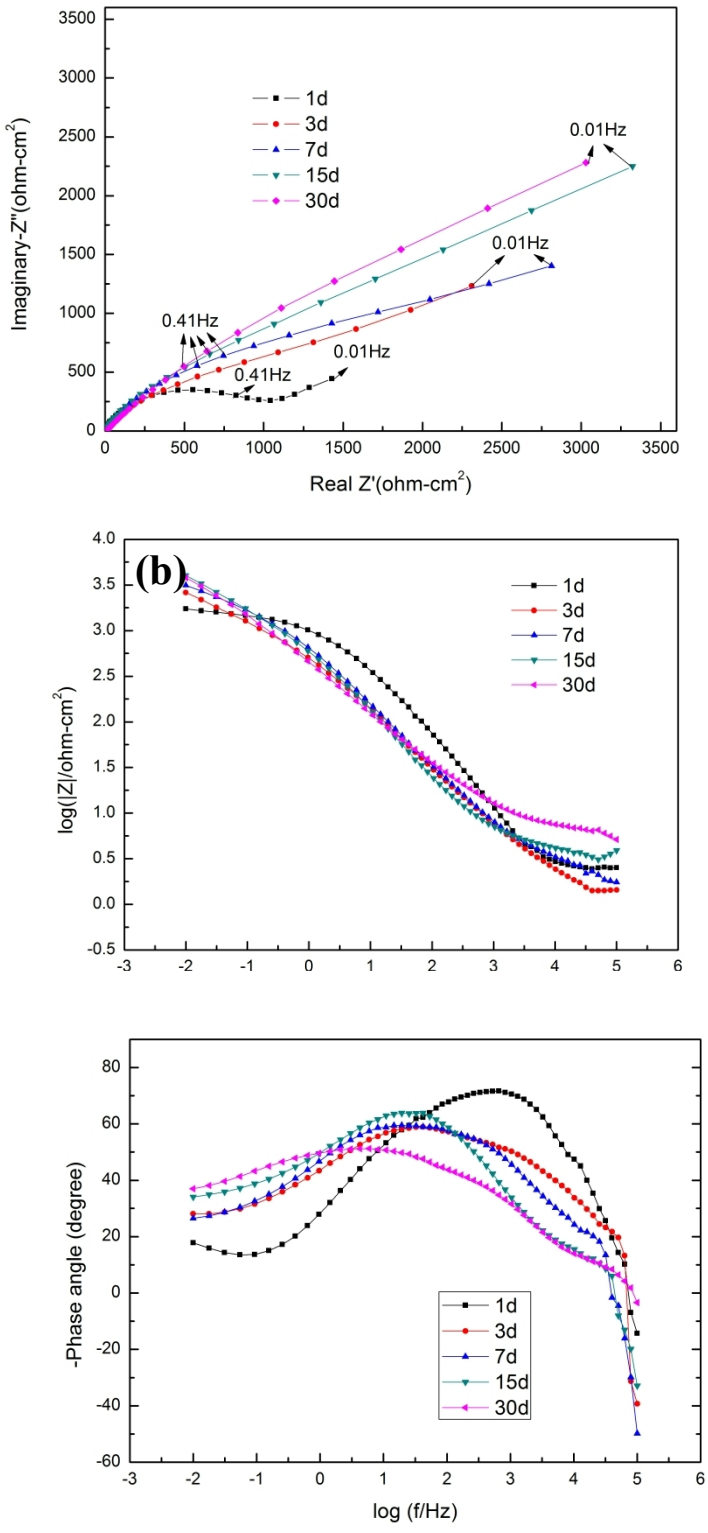

Figure 7 Impedance spectra of TTMT samples exposed in 3.5wt% NaCl solution for different times. (a) Nyquist impedance, (b) Bode impedance and (c) Bode phase angle

3.3.2 XPS analysis

Figure 8 shows the wide XPS spectra of the TTMT sample exposed in 3.5wt% NaCl solution for 1 day and 30 days. The main elements in the corrosion product layer are Cu, O, Sn, Ni, Zn, Al and Cl. Si was not detected due to its low concentration in the alloy. For the specimen exposed in NaCl solution for 1 day, the spectra show strong XPS signals from Cu, O, Al, Cl but the signals of Ni and Sn are very weak. Prolonging the exposure time to 30 days resulted in significant increases in the signals of Ni, Sn and O, indicating increased presence of these elements in the corrosion product layer.

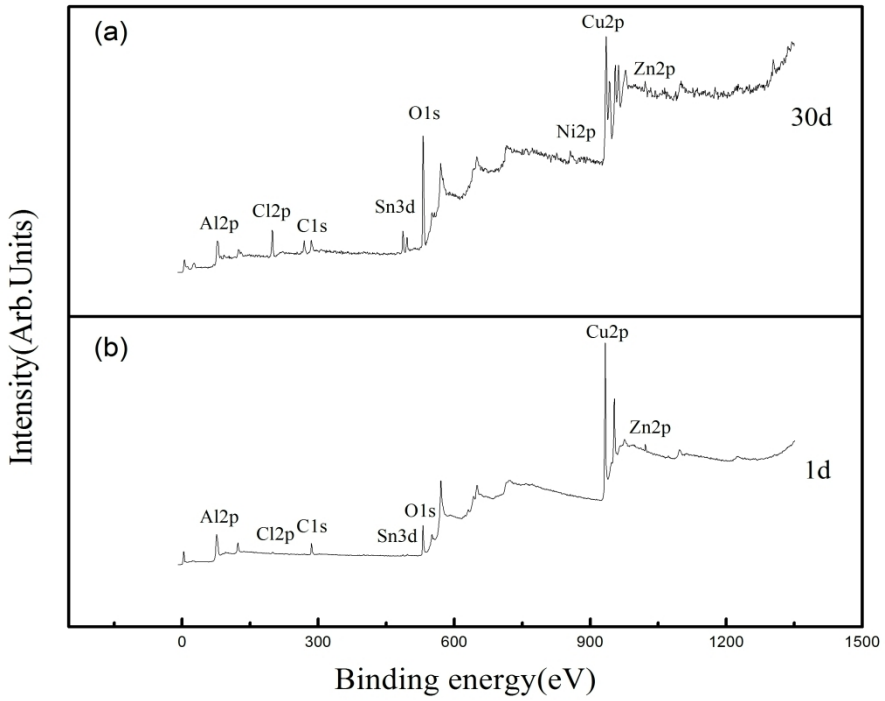

Figure 8 Wide XPS spectra for the surface of the TTMT sample exposed in 3.5wt% NaCl solution for different times

3.3.2.1 Cu2p spectra

Figure 9 shows the Cu2p3/2 spectra of the corrosion products layer. The corrosion

products of the specimen exposed for 1 day are Cu/Cu_2O and CuCl, with their relative quantities of 87% and 13%, respectively. With a prolonged exposure time of 30 days, CuCl was no longer present and CuO and $Cu(OH)_2$ appeared instead. The relative quantity of Cu/CuO_2 decreased to 20%, while the relative quantities of CuO and $Cu(OH)_2$ were increased to 30% and 50%, respectively. These results suggested the formation of a duplex layer on the surface of the alloy after long-time corrosion in NaCl solution, with the inner layer of Cu_2O and the outer layer of a combination of CuO and $Cu(OH)_2$. The transitions of the corrosion products from Cu_2O to CuO, and from CuCl to $Cu(OH)_2$ likely occurred during the corrosion [22].

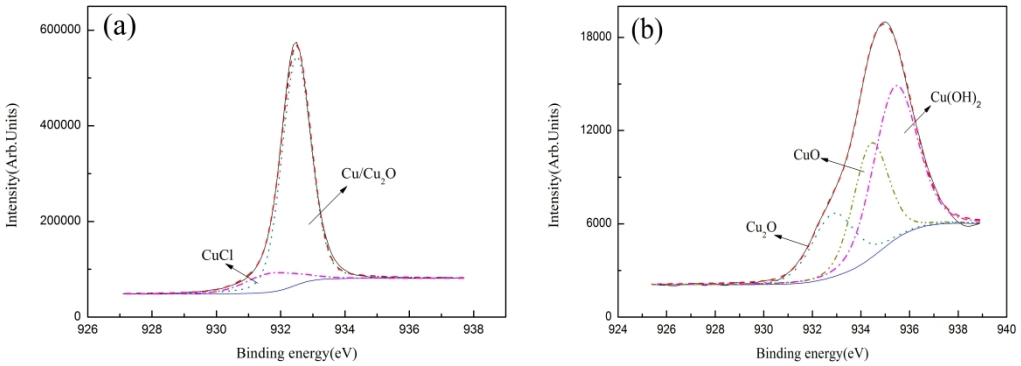

Valence state	Exposure time (days)	Probable compounds	Binding energy (eV)	Intensity area	FWHM (eV)	Relative quantity
Cu2p3/2	1	CuCl	931.7	85407.4	1.86	13%
		Cu/Cu_2O	932.5	593046.7	1.06	87%
	30	Cu_2O	932.7	9578.7	2.11	20%
		CuO	934.4	14571.7	1.69	30%
		$Cu(OH)_2$	935.4	24232.9	2.07	50%

Figure 9 Cu2p XPS spectra of the corrosion product layer of the TTMT sample after

immersion in 3.5wt% NaCl solution for (a) 1 day and (b) 30 days. The table shows the fitted parameters for the spectra.

Figure 10 shows the Cu_{LMM} XPS spectra of the corrosion product layer. In the XPS experiment, Al target with the binding energy of 1486.6 eV was used. The binding energy (*BE*) of Cu can be calculated by: $BE = 1486.6 - KE - \phi$, where *KE* is kinetic energy and ϕ is electric displacement. According to Cu_{LMM} auger linear analysis, the peak position of the binding energy of Cu increased with exposure time, indicating that the degree of oxidation of copper increased.

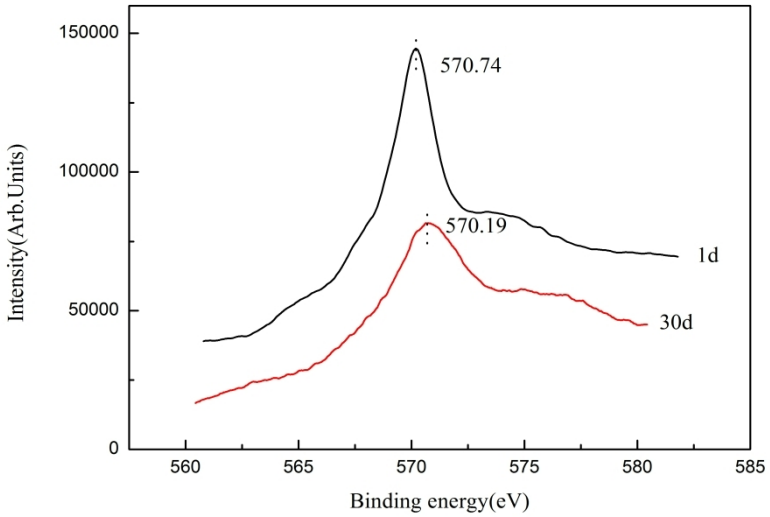

Figure 10 Cu_{LMM} XPS spectra of the corrosion product layer of the TTMT sample exposed in 3.5wt% NaCl solution for different times

3.3.2.2 Ni2p3 spectra

Figure 11 shows the Ni2p3 spectra of the corrosion product layer. Both NiO and $Ni(OH)_2$, with the peaks at 855.9 and 856.6 eV, respectively, were found in the product film. Ni was detected in the 1 day sample, but disappeared in the 30 day

sample. This revealed a process of growth of Ni compounds in the outer layer of the product film during corrosion. The concentrations of NiO or $Ni(OH)_2$ in the corrosion product layer remained the same as the exposure time was extended from 1 day to 30 days. It could be deduced that general corrosion of Ni occurred, forming $NiO/Ni(OH)_2$, with the formation of $Ni(OH)_2$ dominating after long-time corrosion.

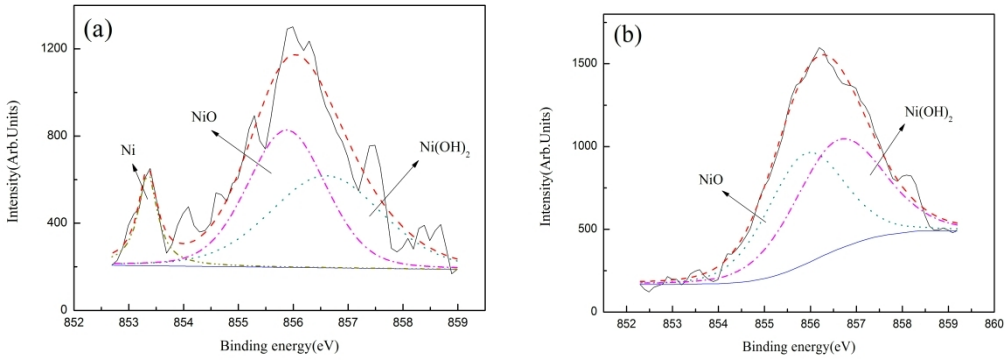

Valence state	Exposure time (days)	Probable compounds	Binding energy (eV)	Intensity area	FWHM (eV)	Relative quantity
Ni2p3	1	Ni	853.4	276.6	0.50	10%
		NiO	855.9	1235.6	1.68	46%
		$Ni(OH)_2$	856.6	1184.2	2.40	44%
	30	NiO	855.9	1530.1	1.97	47%
		$Ni(OH)_2$	856.6	1737.4	2.25	53%

Figure 11 Ni2p XPS spectra of the corrosion product layer of the TTMT sample exposed in 3.5wt% NaCl solution for (a) 1 day and (b) 30 days. The table shows the fitted parameters for the spectra.

3.3.2.3 Sn3p5/2 spectra

Figure 12 shows the core-level Sn3d5/2 spectra of the corrosion product layer. It should be pointed out that the Sn3p5 peak at the same binding energy of 486.4 eV can be attributed to either metallic Sn or SnO due to the difficulty in distinguishing the little difference between them. In addition to Sn/SnO, SnO_2 was also detected in both samples at the peak of 487.4 eV. It seems both SnO and SnO_2 formed at the early stage of corrosion and there was very little change in their concentrations on the surface of corrosion film with prolonging exposure time.

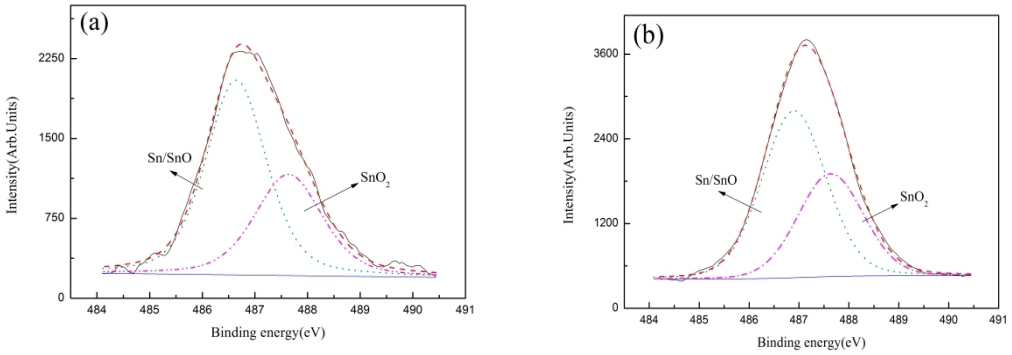

Valence state	Exposure time (days)	Probable compounds	Binding energy (eV)	Intensity area	FWHM (eV)	Relative quantity
Sn3d5	1	Sn/SnO	486.6	3106.12	1.36	63%
		SnO_2	487.4	1810.80	1.51	37%
	30	Sn/SnO	486.6	4060.58	1.50	62%
		SnO_2	487.4	2488.04	1.54	38%

Figure 12 Sn3d XPS spectra of the corrosion product layer of the TTMT sample exposed in 3.5wt% NaCl solution for (a) 1 day and (b) 30 days. The table shows the fitted parameters for the spectra.

3.3.2.4 Zn2p spectra

Figure 13 shows the Zn2p spectra of the corrosion product layer. The two peaks at binding energies of about 1020.8 eV and 1022.2 eV can be attributed to Zn and ZnO, respectively. Both Zn and ZnO were detected on the specimen exposed for 1 day, indicating that ZnO formed at the early stage of corrosion. Similar to the Ni2p3 spectra results, metallic Zn only existed in the 1 day sample. When the exposure time was prolonged to 30 days, only the corrosion product of Zn in the form of ZnO was detected on the surface of the specimen.

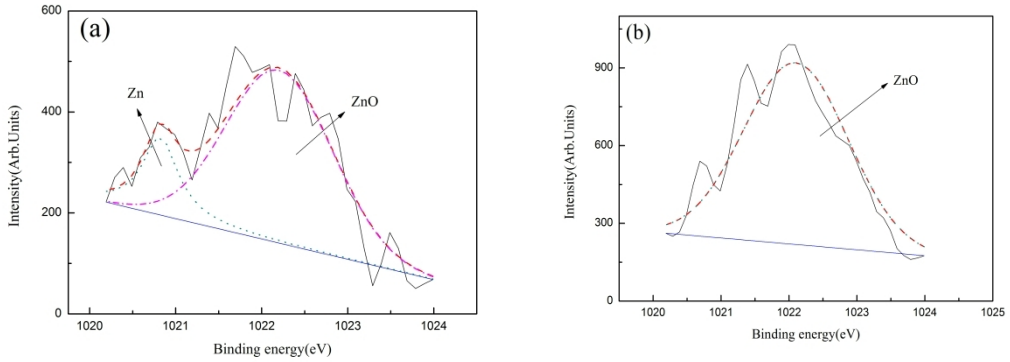

Valence state	Exposure time (days)	Probable compounds	Binding energy (eV)	Intensity area	FWHM (eV)	Relative quantity
Zn2p	1	Zn	1020.8	122.2	0.50	19%
		ZnO	1022.2	533.3	1.46	81%
	30	Zn	-	-	-	-
		ZnO	1022.1	1350.2	1.81	100%

Figure 13 Zn2p XPS spectra of the corrosion product layer of the TTMT sample exposed in 3.5wt% NaCl solution for (a) 1 day and (b) 30 days. The table shows the fitted parameters for the spectra.

3.3.2.5 Al2p spectra

Figure 14 shows the core-level Al2p spectra of the corrosion product layer. Al mainly existed in the forms of Al_2O_3 and $Al(OH)_3$, corresponding to binding energies of 74.2eV and 74.7eV, respectively. Both $Al(OH)_3$ and Al_2O_3 formed at the early stage of corrosion. With a prolonged exposure time of 30 days, however, only Al_2O_3 was detected on the surface of the corrosion layer. It was well documented that the addition of aluminum to copper could improve its corrosion performance in sea water due to the formation of a sustainable protective layer of alumina (Al_2O_3) on the alloy surface [19, 22]. The current results suggested that a protective layer of alumina formed on the surface of the designed alloy during the corrosion process, which played an important role in improving the corrosion resistance of the alloy.

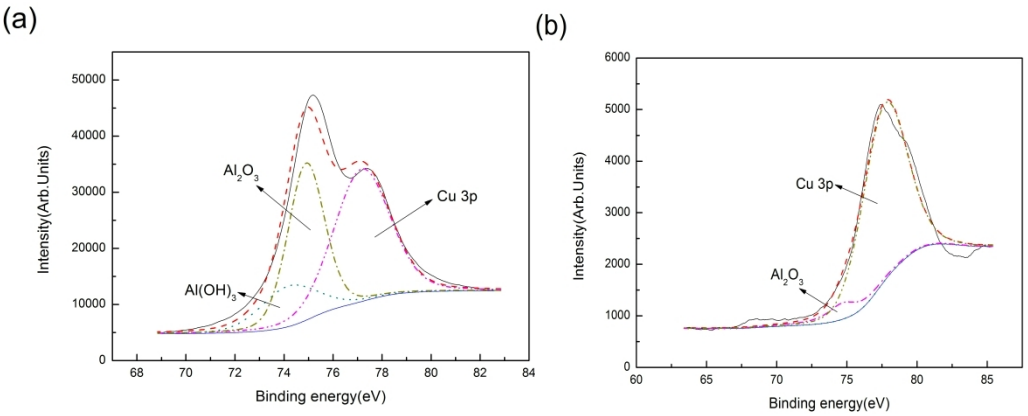

Valence state	Exposure time (days)	Probable compounds	Binding energy (eV)	Intensity area	FWHM (eV)	Relative quantity
Al2p	1	$Al(OH)_3$	74.20	22760.11	2.7	28%
		Al_2O_3	74.7	57788.07	1.77	72%
	30	$Al(OH)_3$	74.20	-	-	-
		Al_2O_3	74.7	1359.11	2.7	100%

Figure 14 Al2p XPS spectra of the corrosion product layer of the TTMT sample

exposed in 3.5wt% NaCl solution for (a) 1 day and (b) 30 days. The table shows the fitted parameters for the spectra.

3.3.2.6 O1s spectra

Figure 15 shows the O1s spectra of the corrosion product layer. They were considered together with the spectra of Cu2p, Ni, Sn, Zn and Al to predict the likely corrosion products. Because the same type of oxides has a similar binding energy, the peaks at the binding energies of 530.5, 531.6 and 532.3 eV could be attributed to MO (CuO/NiO/SnO/ZnO), MO_x ($Cu_2O/SnO_2/Al_2O_3$) and $M(OH)_x$ ($Cu(OH)_2/Al(OH)_3$), respectively. The results are consistent with those shown in Figs. 8, 10, 11, 12 and 13. Based on the analysis of the relative quantities of these corrosion products, there seemed to be a transition from MO_x to MO and $M(OH)_x$ during the corrosion process, which can be confirmed by the Cu spectra and is in agreement with the results obtained from other Cu-Ni alloys [21-22, 26].

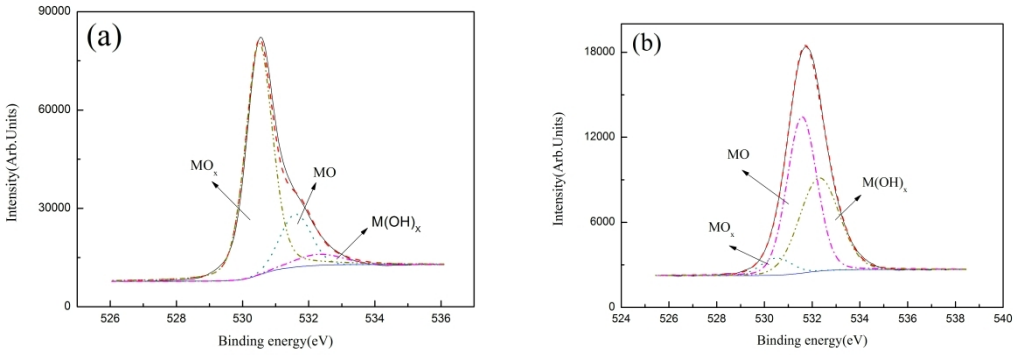

Valence state	Exposure time (days)	Probable compounds	Binding energy (eV)	Intensity area	FWHM (eV)	Relative quantity
O1s	1	MO_x	530.5	82323.4	0.96	77%

	MO	531.6	19019.2	1.11	18%
	$M(OH)_x$	532.3	6170.6	1.72	5%
30	MO_x	530.5	1938.2	1.52	6%
	MO	531.6	18123.5	1.47	53%
	$M(OH)_x$	532.3	14079.5	1.96	41%

Figure 15 O1s XPS spectra of the corrosion product layer of the TTMT sample after immersion in 3.5wt% NaCl solution for (a) 1 day and (b) 30 days. The table shows the fitted parameters for the spectra.

3.3.3 Discussion on sub-processes of corrosion

The XPS results showed that the main corrosion products at the early stage of corrosion were Cu_2O, CuO, CuCl, NiO, $Ni(OH)_2$, SnO, SnO_2, ZnO, Al_2O_3 and $Al(OH)_3$. With prolonged exposure time, the amounts of oxides of Ni, Sn, Zn and Al increased slightly due to continued corrosion of these alloying elements. The most significant changes are that CuCl and $Al(OH)_3$ disappeared and the amount of Cu_2O decreased while the amounts of CuO and $Cu(OH)_2$ increased significantly at the surface. The EIS analysis showed that, with increasing exposure time, the corrosion product layer changed from a single layer to a duplex layer. As XPS only reveals the composition in a very thin corrosion layer, it is reasonable to conclude that the duplex layer consisted of an inner layer of Cu_2O and an outer layer of CuO and $Cu(OH)_2$.

The electrode potentials for reversible anodic dissolution of the alloying elements in the alloy, Al, Zn, Ni and Sn, are -1.662 V, -0.762 V, -0.257 V and -0.138 V, respectively. These elements could be dissolved preferentially at the early stage of the corrosion process due to their negative electrode potentials. Some gas bubbles were

observed to appear on the surface of the tested samples at this stage, so the cathodic reaction was likely to mainly involve the reduction of H^+ and the formation the H_2.

At the early stage of corrosion, aluminum was oxidized to form a porous film of Al_2O_3 [20]. As the solution was slightly alkaline due to the reduction of H^+, some Al^{3+} could bond with OH^- to form $Al(OH)_3$. The precipitated aluminum hydroxide often forms gels, which subsequently crystallize. With increasing exposure time, more Al_2O_3 formed and the film became dense and effective in protecting the alloy.

The alloying elements Zn, Ni and Sn reacted with Cl^- to form chloride complexes, which further reacted with OH^- to form oxides, as shown below:

$$M^2+2Cl^-\rightarrow MCl_2$$

$$MCl_2+2OH^-\rightarrow MO+H_2O+2Cl^-$$

where M represents Zn, Ni or Sn. Some Ni^{2+} could bond with OH^- to form $Ni(OH)_2$. The formation of SnO_2 could also be attributed to:

$$Sn^{2+}\rightarrow Sn^{4+}+2e^-$$

$$Sn^{4+}+4OH^-\rightarrow SnO_2\downarrow+2H_2O$$

The corrosion of Cu-based alloy in NaCl solution often involves the oxidation of Cu and reduction of O_2. The anodic reaction of the designed alloy could be:

$$Cu+Cl^-\rightarrow CuCl+e^-$$

and the cathodic reaction was:

$$O_2+2H_2O+4e^-\rightarrow 4OH^-$$

CuCl could easily be dissolved in the solution and tended to form the cuprous

complex $CuCl^-_2$, which could subsequently react with OH^- to form Cu_2O:

$$CuCl+Cl^- \rightarrow CuCl^-_2$$

$$2CuCl^-_2+2OH^- \rightarrow Cu_2O\downarrow+H_2O+4Cl^-$$

Similar to the corrosion process in Cu-Ni alloys [26-27,31], the Cu_2O formed on the surface of the TTMT sample had P type semiconductor defects. Nickel and other alloying elements could easily be incorporated in these defects, therefore decreasing the electronic conductivity and improving the corrosion resistance [28,29].

Further oxidation of Cu turned Cu_2O to CuO through the reaction below:

$$Cu_2O+O_2+H_2O \rightarrow 2CuO\downarrow+H_2O_2$$

With long exposure time, $Cu(OH)_2$ could also be produced through the reaction:

$$Cu_2O+3H_2O \rightarrow 2Cu(OH)_2\downarrow+2H^++2e^-$$

4.Conclusions

(1) The polarization resistance (R_p) of both the TTMT and STMT samples increased with corrosion time. For any given exposure time, R_p of the TTMT sample was greater than that of the STMT sample. The TTMT sample showed typical uniform corrosion, while localised corrosion was found in the STMT sample.

(2) Coarse, discontinuous Sn- and Ni-rich precipitates formed at the grain boundaries in the STMT sample served as anodes of micro-batteries, resulting in localised corrosion due to galvanic corrosion. A large number of nano-scale precipitates were formed during pre-aging in the TTMT sample. During cold deformation, they interacted with dislocations to produce a large quantity of dislocation tangles, which provided a large number of nucleation sites and led to uniform distribution of fine

precipitates during subsequent aging. As a consequence, the TTMT sample had better corrosion resistance performance than the STMT sample.

(3) The corrosion product layer formed on the surface of the alloy mainly contained Cu_2O, CuO, NiO, $Ni(OH)_2$, SnO, SnO_2, ZnO and Al_2O_3. With increasing exposure time, the corrosion products changed from Cu_2O to CuO and $Cu(OH)_2$. Aluminum was oxidized to form a dense oxide film, which to some extent protected the alloy from corrosion.

(4) A duplex layer consisting of an inner layer of Cu_2O and an outer layer of CuO and $Cu(OH)_2$ was responsible for the good corrosion resistance of the alloy.

Acknowledgement

The authors acknowledge the financial support by the National Natural Science Foundation of China (Grant No. 51601227), National Key Research and Development Program of China (2016YFB0301300), China Postdoctorates Science Foundation (Grant No. 2016M590753), and grants from the Project of Innovation-Driven Plan and the Project of State Key Laboratory of Powder Metallurgy, Central South University, Changsha, China.

References

[1] Sahu P, Pradhan S K, De M. X-ray diffraction studies of the decomposition and microstructural characterization of cold-worked powders of Cu–15Ni–Sn alloys by Rietveld analysis, Journal of Alloys & Compounds. 377 (1-2) (2004) 103-116.

[2] Caris J, Li D, Jr J J S, et al., Microstructural effects on tension behavior of Cu–15Ni–8Sn sheet, Materials Science & Engineering A. 27 (3) (2010) 769-781.

[3] Yu W U, Yang S L. Research and Development Prospect of High-elastic Cu-Ni-Sn Alloy, Shanghai Nonferrous Metals. 35 (1) (2004) 38-43.

[4] Zhao J C, Notis M R. Spinodal decomposition, ordering transformation, and discontinuous precipitation in a Cu–15Ni–8Sn alloy, Acta Materialia. 46 (12) (1998) 4203-4218

[5] Miki M, Ogino Y. Effect of Si Addition on the Cellular Precipitation in a Cu–10Ni–8Sn Alloy, Materials Transactions. 31 (1990) 968-974.

[6] Souissi N, Sidot E, Bousselmi L, et al., Corrosion behaviour of Cu–10Sn bronze in aerated NaCl aqueous media – Electrochemical investigation, Corrosion Science. 49 (8) (2007) 3333-3347.

[7] Deyong L, Elboujdaïni M, Tremblay R, et al., Electrochemical behavior of rapidly solidified and conventionally cast Cu-Ni-Sn alloys, Journal of Applied Electrochemistry. 20 (5) (1990) 756-762.

[8] Graedel T E, Plewes J T, Franey J P, et al., Sulfidation under atmospheric conditions of Cu-Ni, Cu-Sn, and Cu-Zn binary and Cu-Ni-Sn and Cu-Ni-Zn ternary systems, Metallurgical & Materials Transactions A. 16 (1) (1985) 275-284.

[9] Lin Y C, Zhang J L, Liu G, et al., Effects of pre-treatments on aging precipitates and corrosion resistance of a creep-aged Al–Zn–Mg–Cu alloy[J], Materials & Design. 83 (2015) 866-875.

[10] Li Q, Li J, Ma G, et al., Influence of ω phase precipitation on mechanical

performance and corrosion resistance of Ti–Nb–Zr alloy[J], Materials & Design. 111 (2016) 421-428.

[11] Kratochvíl P, Mencl J, Pešička J, et al., The structure and low temperature strength of the age hardened Cu-Ni-Sn alloys, Acta Metallurgica. 32 (84) (1984) 1493–1497

[12] Helmi F M, Zsoldos L. On the thermal decomposition of Cu-Ni-Sn after prior cold-work, Scripta Metallurgica. 11 (10) (1977) 899-901

[13] Spooner S, Lefevre B G. The effect of prior deformation on spinodal age hardening in Cu-15Ni-8Sn alloy, Metallurgical & Materials Transactions A. 11 (7) (1980) 1085-1093.

[14] Donoso E, Diánez M J, Perejón A, et al., Microcalorimetry: A powerful tool for quantitative analysis of aging hardening response of Cu-Ni-Sn alloys, Journal of Alloys and Compounds. 694 (2017) 710-714.

[15] Diánez M J, Donoso E, Sayagués M J, et al., The calorimetric analysis as a tool for studying the aging hardening mechanism of a Cu-10wt% Ni-5.5 wt% Sn alloy, Journal of Alloys and Compounds. 688 (2016) 288-294.

[16] Singh J B, Wen J G, Bellon P. Nanoscale characterization of the transfer layer formed during dry sliding of Cu–15wt.% Ni–8wt.% Sn bronze alloy, Acta Materialia. 56 (13) (2008) 3053-3064.

[17] Wang Y, Zhang L, Xiao J, et al., The tribo-corrosion behavior of Cu-9wt% Ni-6wt% Sn alloy, Tribology International. 94 (2016) 260-268.

[18] Lei Q, Li Z, Han L, et al., Effect of aging time on the corrosion behavior of a Cu-Ni-Si alloy in 3.5 wt. % NaCl solution, Corrosion -Houston Tx-. 72 (5) (2016) 615-627

[19] Yuan S J, Pehkonen S O. Surface characterization and corrosion behavior of

70/30 Cu–Ni alloy in pristine and sulfide-containing simulated seawater, Corrosion Science. 49 (3) (2007) 1276-1304.

[20] Xiao Z, Li Z, Zhu A, et al., Surface characterization and corrosion behavior of a novel gold-imitation copper alloy with high tarnish resistance in salt spray environment, Corrosion Science.76 (2) (2013) 42-51.

[21] Zhu X, Lei T. Characteristics and formation of corrosion product films of 70Cu–30Ni alloy in seawater, Corrosion Science. 44 (1) (2002) 67-79.

[22] Milošev I, Metikoš-Huković M. The behaviour of Cu-xNi (x = 10 to 40 wt%) alloys in alkaline solutions containing chloride ions, Electrochimica Acta. 42 (10) (1997) 1537–1548.

[23] Alili B, Bradai D, Zieba P. On the discontinuous precipitation reaction and solute redistribution in a Cu-15%Ni-8%Sn alloy, Materials Characterization. 59 (10) (2008) 1526-1530.

[24] Fonda R W, Shiflet G J. Atomic growth mechanisms for lamellar structures, Ultramicroscopy. 30 (1) (1989) 116–131.

[25] Odnevall Wallinder I, Zhang X, Goidanich S, et al., Corrosion and runoff rates of Cu and three Cu-alloys in marine environments with increasing chloride deposition rate, Science of the Total Environment. 472C (2014) 681-694.

[26] Ismail K M, Fathi A M, Badawy W A. The Influence of Ni Content on the Stability of Copper—Nickel Alloys in Alkaline Sulphate Solutions, Journal of Applied Electrochemistry. 34 (8) (2004) 823-831.

[27] Druska P, Strehblow H H. Surface analytical examination of passive layers on Cu-Ni alloys part II, Acidic solutions. Corrosion Science. 38 (8) (1996) 1369-1383.

[28] Blundy R G, Pryor M J. The potential dependence of reaction product composition on copper-nickel alloys, Corrosion Science. 12 (1) (1972) 65-75.

[29] North R F, Pryor M J. The influence of corrosion product structure on the corrosion rate of Cu-Ni alloys, Corrosion Science. 10(5) (1970) 297-311.

[30] K.D. Ralston, N. Birbilis, M. Weyland, C.R. Hutchinson. The effect of precipitate size on the yield strength-pitting corrosion correlation in Al–Cu–Mg alloys, Acta Materialia. 58 (18) (2010) 5941-5948.

[31] J.L. Chen, Z. Li, A.Y. Zhu, L.Y. Luo, J. Liang, Corrosion behavior of novel imitation-gold copper alloy with rare earth in 3.5% NaCl solution, Materials and Design. 34 (2012) 618–623.